

INDENTATION TOUGHNESS OF Al_2O_3 -CNT NANOCOMPOSITES

VIKTOR PUCHÝ^{a,*}, JÁN DUSZA^a, FAWAD INAM^b, and MICHAEL J. REECE^b

^a Institute of Materials Research, Slovak Academy of Sciences, Watsonova 47, 04353 Košice, Slovakia, ^b Centre for Materials Research and School of Engineering and Materials Science, Queen Mary, University of London, Mile End Road, London E1 4NS, UK
vpuchy@imr.saske.sk

Keywords: indentation toughness, Al_2O_3 , carbon nanotube, carbon black

1. Introduction

In the last few years new ceramic/carbon nanotube composites have been developed and a number of authors have reported improved mechanical and functional properties in the case of ceramic/CNT composites compared to the monolithic materials¹. According to the results reinforcing by CNTs in many cases improved the fracture toughness of Al_2O_3 , however, this toughening is not evident, and some of the variations may purely arise from using different testing techniques². The improvement in fracture toughness is due to bridging of the crack surfaces by CNTs during the crack propagation by CNT pullout mechanism, which strongly depends on the interfacial bonding between CNTs and the matrix.

The aim of the present work is to investigate the effect of addition of carbon nanotubes and carbon black on the indentation toughness of alumina-CNT and alumina-carbon black nanocomposites.

2. Experimental materials and methods

The experimental materials were prepared by spark plasma sintering at the Queen Mary University of London³.

The microstructure and fracture surfaces of the investigated materials were studied using scanning electron microscopy (SEM). The small specimen size did not allowed to use standard fracture toughness test, therefore indentation fracture toughness test was performed at loads of 50 and 100 N using a Vickers indenter, and the calculation were made using Anstis equation:

$$K_{\text{IC}} = 0.016 \left(\frac{E}{H} \right)^{1/2} \left(\frac{P}{c^{3/2}} \right)$$

where E is the modul of elasticity, H is the hardness and c the radial crack length generated by Vickers's indentation. At least 10 indentation have been made for all investigated materials. The grain size was measured on polished/etched surface and fracture surface of specimens using standard statistical methods.

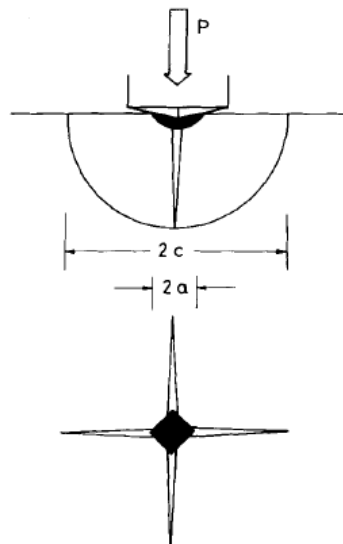


Fig. 1. Schematic illustration of the indentation cracks used for the calculation of the indentation toughness

3. Results and discussion

The microstructure of the monolithic Al_2O_3 consists of large, micron sized grains with randomly placed submicrometer sized pores. The grain size of the matrix is lower in the $\text{Al}_2\text{O}_3 + 2\%$ CB composite and even lower in the $\text{Al}_2\text{O}_3 + 5\%$ CB composite. Relatively large numbers of CNF clusters were observed on the polished and fracture surfaces of the $\text{Al}_2\text{O}_3 + 5\%$ CNT composites. This material has even finer matrix with relatively well distributed carbon nanotubes with diameter several of nanometers and very high aspect ration. The smaller matrix grain size in the composite suggests that the carbon black and the CNTs hinder the grain growth during the sintering.

The CNTs in the Al_2O_3 -CNT composite were located mainly in the intergranular places and they were well attached to the alumina grains.

The indentation toughness of monolithic alumina is approximately $3.25 \text{ MPa m}^{1/2}$ which is comparable with similar materials in the literature. The addition of 2% carbon black increased the indentation toughness, but after increasing to 5% decreased to the similar level as the indentation toughness of monolithic material. The addition of 5% CNTs increased the indentation toughness up to $4.14 \text{ MPa m}^{1/2}$ which is the highest value obtained for the materials investigated.

Well-dispersed CNT-reinforced Al_2O_3 nanocomposites have been recently prepared with reasonably high density using hot pressing⁴. According to the results 2 wt.% of CNT addition increased the hardness, flexural strength and fracture toughness of nanocomposites (from 3 to $4.3 \text{ MPa m}^{1/2}$), how-

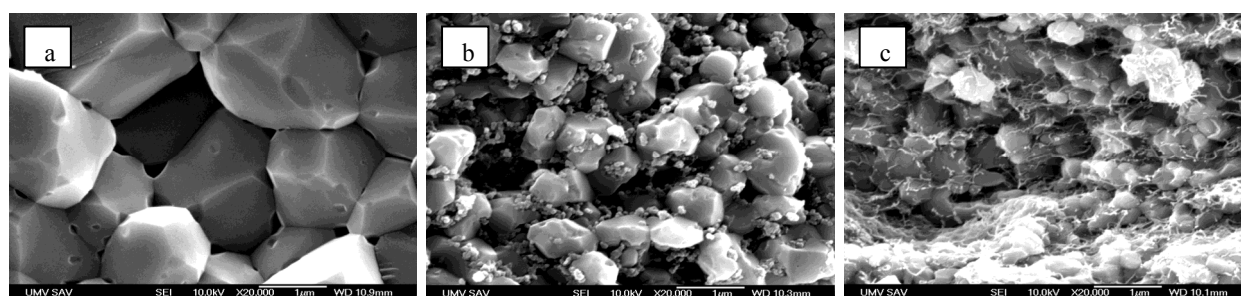


Fig. 2. Microstructure of the investigated materials, Al₂O₃ (a), Al₂O₃ + 5 % CB (b) and Al₂O₃ + 5 % CNT (c)

Table I
Indentation toughness and grain size of investigated materials

Sample	K_{IC} [MPa m ^{1/2}]	Grain size [nm]
Al ₂ O ₃	3.24 ± 0.15	1802 ± 339
Al ₂ O ₃ + 2 % CB	3.84 ± 0.5	1065 ± 120
Al ₂ O ₃ + 5 % CB	3.44 ± 0.25	536 ± 61
Al ₂ O ₃ + 5 % CNT	4.14 ± 0.62	383 ± 45

ever further CNT addition up to 5 wt.% slightly decreased the hardness, reduced the flexural strength but improved the toughness up to 4.5 MPa m^{1/2}. The increase in toughness is believed to be associated with the strong interface connections between the CNT and the matrix, resulting in pullout resistance, bridged the crack gaps and hindered the crack propagation by exploiting CNTs elasticity, leading to improved fracture toughness.

In monolithic alumina the toughening mechanisms during the crack propagation are in bridging zone of the propagating crack in the form of frictional and mechanical bridges arising as a result of crack deflection at the Al₂O₃/Al₂O₃ boundaries. These toughening mechanisms are effective in large grain sized ceramics and by decreasing grain size are less important. From this is evident that in composites, investigated in this study, for the improved indentation toughness different toughening mechanisms are responsible. These are probably the carbon based bridges between the alumina grains, which mainly in the case of Al₂O₃ + CNT composite are strong enough to increase the resistance against the crack propagation. These results are in good agreement with the results of recent investigations.⁴

4. Conclusion

The effect of addition of carbon nanotubes and carbon black on the mechanical properties of alumina-CNT and alumina-carbon black nanocomposites has been investigated. The addition of carbon black decreased and approximately 20 %. The increased toughness is probably connected with the interfacial bonding between the CNTs and the matrix and with the bridging effect of the CNTs during the crack propagation.

This work was partly supported by APVV LPP-0174-07, APVV-0034-07, VEGA No. 2/0088/08 and MNT-ERA.NET HANCOC.

REFERENCES

1. Hirota K., Takaura Y., Kato M. and Miyamoto Y.: *J. Mater. Sci.* **42**, 4792 (2007).
2. Padture N. P.: *Adv. Mater.* **21**, 1767 (2009).
3. Fawad I., Haixue Y., Daniel D. J., Peijs T., Reece M. J.: *J. Eur. Ceram. Soc.* **30**, 153 (2010).
4. Ahmad, Unwin M., Cao H., Chen H., Zhao H., Kennedy A., Zhu Y. Q.: *Comp. Sci. Technol.* **70**, 1199 (2010).

V. Puchý^a, J. Dusza^a, P. Hvizdoš^a, F. Inam^b, and M. Reece^b (^aIMR SAS Košice, Slovakia, ^bUniversity of London, UK): **Indentation Toughness of Al₂O₃-CNT Nanocomposites**

Indentation toughness behavior of Al₂O₃ based nanocomposites with addition of carbon nanotubes and carbon black prepared by spark plasma sintering (SPS) has been studied by Vickers indentation technique. Vickers hardness and cracks were measured and recorded, indentation toughness were calculated. The microstructure, CNT/CB dispersion and fracture surface were studied using optical and electron microscopy and its mechanisms were identified.

NANOSCALE DYNAMIC MECHANICAL ANALYSIS OF SOFT TISSUE AND ITS FINITE ELEMENT MODELING

JOSEF ŠEPITKA*, JAROSLAV LUKEŠ, JIŘÍ KUŽELKA, and JAN ŘEZNÍČEK

Czech Technical University in Prague, Faculty of Mechanical Engineering, Dep. of Mechanics, Biomechanics and Mechatronics, Technická 4, 166 07 Prague 6, Czech Republic
Josef.Sepitka@fs.cvut.cz

Keywords: nanoindentation, end plate, nanoDMA, intervertebral disc, FEM

1. Introduction

According to recent studies the nanoindentation seems to be very effective tool to analyze mechanical properties of biomaterials especially in case of hardly accessible soft tissue. Machining of biological material to normalized shaped samples for tensile testing is quite difficult

This paper presents a study of implementing the experimental data from nanoscale dynamical mechanical analysis (nanoDMA) of bovine intervertebral end plate (EP) to the material library of commercial software Abaqus and nanoDMA experiment modeling.

1.1. End Plate

Cartilaginous end plate (EP) (Fig. 1) is a part of intervertebral disc that creates the transition zone between hard vertebral body and soft annulus fibrosus (AF). The process of calcification within AF lamellae and EP is crucial for mechanical behavior of intervertebral disc. It is observed as the clinical syndrome in childhood and elderly population. Sometimes the etiology is unclear. The previous trauma, surgical intervention or overloading are suggested. Calcification of end plate has critical influence on salute flow to avascular annulus fibrosus end nucleus pulposus and initiates the IVD degeneration¹. Nanoindentation is an experimental method, which can tell us more about tissue mechanics of end plate².

2. Methods

2.1. Samples preparation

Sagittally halved bovine spine was obtained from the butchery. The lumbar spine motion segments were immediately dissected and five millimeter thick plates of vertebral body, end plate and annulus fibrosus were cut and polished under running water condition. Samples were placed into the physiological solution right after. The plate of the sample was glued to the bottom of the Petri dish and surrounded by physiological solution again. The surface was water free and ready to be indented.

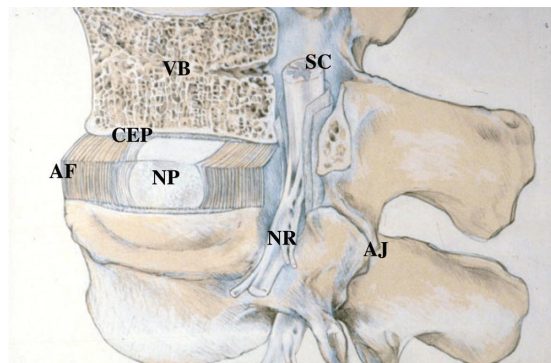


Fig. 1. A schematic view of a spinal segment and the intervertebral disc. The figure shows the organization of the disc with the nucleus pulposus (NP) surrounded by the lamellae of the annulus fibrosus (AF) and separated from the vertebral bodies (VB) by the cartilaginous end-plate (CEP). The figure also shows the relationship between the intervertebral disc and the spinal cord (SC), the nerve root (NR), and the apophyseal joints (AJ). Adopted from Urban et al. (2004)¹

2.2. Testing conditions

NanoDMA load controlled experiment was performed with Hysitron TriboIndenter™ system with Berkovich diamond tip at the temperature 21.4 °C.

Harmonic loading $P_0 = \sin(\omega t)$ with dynamic load amplitude $P_0 = 20 \mu\text{N}$ was specified for the harmonic frequency range 5–295 Hz. During nanoDMA experiment was applied static load with maximum force $P_{max} = 800 \mu\text{N}$. That corresponded to the contact indentation depth $h_c = 360.49 \pm 129.73 \text{ nm}$. Configuration of measurement was assumed from Lukeš et. al. (2010)³ The amplitude of the displacement oscillation X_0 and Φ the phase shift of the displacement with respect to the driving force are recorded by the nanoindentation system. The machine compliance C_i and the stiffness value K_i were determining during air indent calibration. The procedure was adopted from Asif et. al. (1999)⁴ as well as the analysis of dynamic data.

The reduced storage modulus (E_r'), the storage loss modulus (E_r'') and $\tan \delta = E_r'/E_r''$ depending on compliance and stiffness of the sample are given by

$$E_r' = \frac{K \sqrt{\pi}}{2\sqrt{A}} \quad E_r'' = \frac{\omega C_s \sqrt{\pi}}{2\sqrt{A}} \quad \text{and} \quad \tan \delta = \frac{C_s \omega}{K_s}$$

where A is the contact area based on tip area function related to the contact depth at quasistatic loading⁵. The storage and loss modulus of the sample E_s' and E_s'' , respectively, are related to the reduced storage and loss modulus by

$$\frac{1}{E_r'} = \frac{(1-\nu_i^2)}{E_i} + \frac{(1-\nu_s^2)}{E_s'} \quad \text{and} \quad \frac{1}{E_r''} = \frac{(1-\nu_i^2)}{E_i} + \frac{(1-\nu_s^2)}{E_s''}$$

where subscripts i and s refer to the indenter and sample materials, respectively, and ν is the Poisson's ratio.

The storage modulus and the loss modulus are related to the complex modulus $E_s^* = E_s' + iE_s''$ and indicate the ability of the sample to store and return energy (recoverable deformation; E_s') and dissipate energy (E_s''). The ratio of the loss modulus to the storage modulus (i.e., $\tan \delta$) reflects the viscoelastic behavior of the material. It is a material parameter independent of the tip-sample contact area.

3. Numerical methods

3D FEM model was created for a verification of the nanoDMA method. The model was composed by the sample and Berkovich tip. Commercial software Abaqus 6.9.2 was used for modeling and analysis. The sample was modeled as compliant cylinder with elastic modulus $E = 2$ GPa and with Poisson's ratio $\nu = 0.4^2$. Indenter tip was modeled as discrete rigid material. Tip radius was $R = 100$ nm. Hundred micron deep indent was simulated in the first step (quasistatic pre-load). Harmonic loading was applied on indenter tip using displacement amplitudes in the range of frequencies, which we measured by the nanoDMA experiment. Calculations were using perturbation steps (steady oscillations were solved).

Two material models were defined. The first model considered deviatoric components of deformation only and the second model considered deviatoric and volumetric components of deformation.

4. Results and conclusions

FEM calculation data correlated with nanoDMA experimental data that is shown in the Fig. 2. Figure 2. indicates an agreement between model and experiment in obtained data $\tan \delta$ vs. frequency. $\tan \delta$ represents ratio of loss modulus and storage modulus. The imaginary and real parts of reaction forces correspond to these moduli in FEM analysis. The first material model that was defined for numerical simulation (deviatoric components of deformation only) is not in such an agreement as the second material model (deviatoric and volumetric components of deformation). A friction was not included in FEM simulation which could be explanation of difference between nanoDMA experiment and FEM simulation. It is possible to implement the experimental data to the Abaqus library successfully.

This work was supported by the Grant Agency of the Czech Technical University in Prague, grant No. SGS10/247/OHK2/3T/12.

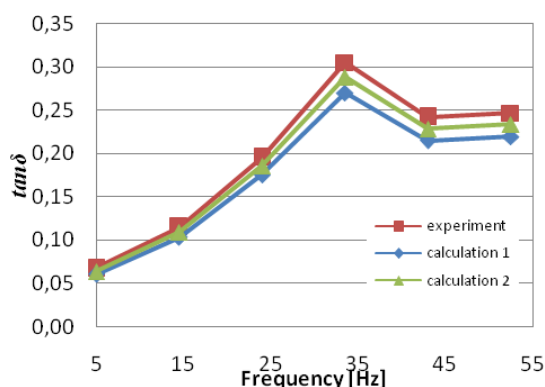


Fig. 2. Loss tangent vs. frequency. Comparison of the experiment data with the FEM calculation

REFERENCES

- Urban J. P. G., Roberts S.: *Arthritis Res. Therapy* 5, 120 (2003).
- Lukes J., Mares T., Nemecek J., Otahal S.: *IFMBE Proceedings* 23, 1792 (2009).
- Lukeš J., Šepitka J., Němeček J.: *Chem. Listy* 104, s341 (2010).
- Asif S. A. S., Wahl K. J., Colton R. J.: *Rev. Sci. Instrum.* 70, 2408 (1999).
- Oliver W. C., Pharr G. M.: *J. Mater. Res.* 7, 1564 (1992).

J. Šepitka, J. Lukeš, J. Kuželka, and J. Řezníček
(Czech Technical University in Prague, Faculty of Mechanical Engineering): **Nanoscale Dynamic Mechanical Analysis of Soft Tissue and Its Finite Element Modeling**

Hysitron Triboindenter™ TI950 system has been used for studying the viscoelastic properties of bovine intervertebral disc's end plate (EP) by means of nanoscale mechanical dynamic analysis (nanoDMA). NanoDMA offers several testing modes in which is a harmonic function prescribed to the indentation force $P(t) = P_0 \sin \omega t$. The resultant displacement amplitude [nm] and phase shift are measured. Then the storage (E') and loss (E'') moduli can be calculated as well as their ratio $\tan \delta$ and complex modulus (E^*). These parameters provide the viscoelastic description of our tissue. NanoDMA experimental data were used for Abaqus material card creation and were employed to the mathematical simulation of nanoDMA experiment.

NANOINDENTATION OF VERY THIN HARD COATINGS

**JOSEF ŠEPITKA*, JAROSLAV LUKEŠ,
VLADIMÍR JECH, FRANTIŠEK ČERNÝ,
and JAN ŘEZNÍČEK**

*Czech Technical University in Prague, Faculty of Mechanical Engineering, Dep. of Mechanics, Biomechanics and Mechatronics, Technická 4, 166 07 Prague 6, Czech Republic
Josef.Sepitka@fs.cvut.cz*

Keywords: nanoindentation, DLC, partial unloading

1. Introduction

Nanoindentation technique is being widely used for measuring intrinsic mechanical properties of hard thin coating. However, we are limited by the size of tip radius, geometry of tip, system sensitivity, quality of sample's surfaces etc. How does the rule of 1/10 rule (EN ISO 14577-1:2002) influence our testing? Does this rule take into the account different tip geometry?

This paper presents a study of actual limits for nanoindentation of very thin coating by two types of diamond tips.

2. Methods

2.1. Samples preparation

Multilayer surface was deposited on tool steel known as a Vanadis to increase wear resistance. TiN coating (50 nm) was deposited by IBAD (Ion Beam Assisted Deposition) method for the improvement of the adhesion of the very top layer of carbon (100 nm). High-voltage device (90 keV) was used for IBAD method for TiN deposition. Then low-energy device (1 keV) was employed for deposition of carbon coating. Ion Beam Mixing (IBM, 90 keV) method was applied on samples to improve the adhesion. IBM mixes the atoms from separate layers and substrate as well. However, it also sputters the surface, which reduces the final thickness of the coatings <150 nm in our case¹. Our thin coating was approximately 100 nm thick. Thickness was measured by Si quartz during deposition.

2.2. Testing conditions

Quasistatic load controlled experiments were performed on Hysitron TriboIndenter™ system with fluid Berkovich and Cube Corner diamond tips using a partial unloading function² consisting of 100 cycles, each composed by loading segment, dwell and unloading segment (1×2×1 second) with maximum force $P_{max} = 7300 \mu\text{N}$ (Fig. 1) and $P_{max} = 3000 \mu\text{N}$, respectively for Berkovich and Cube Corner tip, respectively. Applied loads corresponded to the contact indentation depths $h_c =$

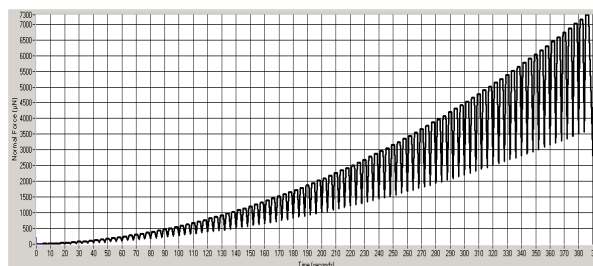


Fig. 1. Load-displacement graph of the nanoindentation for partial unloading function that consists from 100 cycles using for Berkovich tip

$145 \pm 15 \text{ nm}$ at the temperature $22.6 \text{ }^\circ\text{C}$. The grids of 7×7 indents with $5 \mu\text{m}$ separation were applied on four areas for each tip (392 indents overall).

2.3. Quasistatic indentation

Elastic modulus (E_r) is determined from the unloading segment of indentation curve.

$$E_r = \frac{\sqrt{\pi}}{2} \frac{S}{\sqrt{A}} \quad (1)$$

where E_r is reduced modulus, A is contact area and S is measured stiffness. Hardness is defined:

$$H = \frac{P_{max}}{A} \quad (2)$$

where P_{max} is the peak of indentation load and A is the projected area of the tip imprint³.

Tip area functions were made for both tips on the fused quartz sample³ by fitting the A vs. h_c to the relationship implemented to TriboScan's software:

$$A(h) = C_0 h_c^2 + C_1 h_c^1 + C_2 h_c^{1/2} + C_3 h_c^{1/4} + C_4 h_c^{1/8} + C_5 h_c^{1/16} \quad (3)$$

where $C_0 = 24.5$ stands for Berkovich and $C_0 = 2.598$ for Cube Corner tip, respectively. We fitted the polynomial function $A(h)$ (3) with C_{0-4} and C_{0-3} for Berkovich and Cube Corner tip, respectively.

3. Results

Both tips, Berkovich and Cube Corner tip area functions (3) were obtained according to ISO 14577 using the known material parameters (E_r , H) for fused quartz $E_r = 69.6 \text{ GPa}$ and hardness $H = 9.25 \text{ GPa}$. The average values from our calibration procedure were: $E_r = 68.47 \pm 4.69 \text{ GPa}$ and hard-

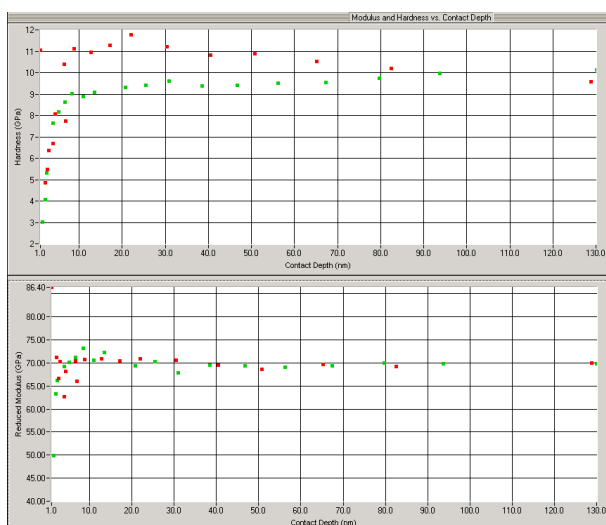


Fig. 2. Modulus and Hardness vs. Contact Depth Berkovich (green) and Cube Corner (red) tip obtained for fused quartz as calibration of area function

ness $H = 8.56 \pm 1.98$ GPa and $E_r = 69.39 \pm 5.57$ GPa and hardness $H = 7.54 \pm 2.85$ GPa for Berkovich and Cube Corner tip, respectively, from 1 to 192 nm of contact depths (Fig. 2).

4. Discussion and conclusion

Cube corner tip is more suitable for measuring of a reduced elastic modulus E_r of a very thin coating than Berkovich tip. If we look at the Fig. 3, cube corner data are stable for the range of depths 10 to 40 nm which means that there is no influence of substrate. Berkovich tip data were unaffected in the range from 10 to 15 nm only. The values of E_r in these ranges for both tips are reliable intrinsic properties of our thin coating because the tip area calibration uses the E_r data measured on fused quartz. However the values of hardness from dataset obtained by cube corner were already higher than expected values of hardness for fused quartz (Fig. 2). It means that cube corner is not ideal for measuring the hardness except for very thin films, where Berkovich indenter cannot be applied due to either very shallow indents (no development of plastic deformation) or immediate influence of substrate (unsatisfaction of 1/10 rule). Fig. 3 shows that the substrate effect starts influencing the results at depth 15 nm for Berkovich and at 40 nm for Cube corner tip in case of our thickness of coating 100 nm. It means that nanoindentation with Berkovich tip has to really respect the rule of 1/10. Sharper Cube corner indenters are usable for thinner coating than 100 nm because the plastic deformation is developed even for very shallow indents and plastic zone beneath the tip is smaller which means that the influence of substrate comes later on in deeper depths.

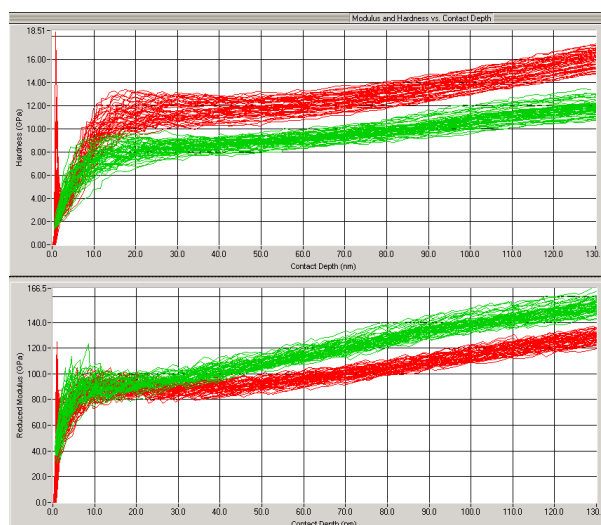


Fig. 3. Modulus and Hardness vs. Contact Depth Berkovich (green) and Cube Corner (red) tip obtained for the sample for 1–130 nm depth

This research work was supported by the Ministry of Education project: Transdisciplinary research in Biomedical Engineering II. No. MSM 6840770012.

REFERENCES

- Černý F., Pitter J., Konvičková S., Jech V.: Surf. Coat. Technol. 203, 2566 (2009).
- Dietiker M., Nyilas R. D., Solenthaler Ch., Spolenak R.: Acta Mater. 230, 499 (2004).
- Oliver W. C., Pharr G. M.: J. Mater. Res. 7, 1564 (1992).

J. Šepitka, J. Lukeš, V. Jech, F. Černý, and J. Řezníček (Czech Technical University in Prague, Faculty of Mechanical Engineering): **Nanoindentation of Very Thin Hard Coatings**

Nanoindentation technique is being widely used for measuring intrinsic mechanical properties of hard thin coating. However, what are the limits of the nanoindentation methods if we have to follow 1/10 rule according to EN ISO 14577-1:2002. How we can analyse very thin coatings about 100 nm thicknesses if we have to follow that rule? We are limited by the size of tip radius, system sensibility, quality of sample surfaces etc. Our paper will be focused on these limits of nanoindentation technique.

EVALUATION OF LOCAL MECHANICAL PROPERTIES IN P23/P91 DISSIMILAR WELDS AFTER CREEP EXPOSURE AT 500–600 °C

LUCIE STRÍLKOVÁ*, **ZDENĚK KUBOŇ**,
and **VLASTIMIL VODÁREK**

*MATERIALS AND METALLURGICAL RESEARCH Ltd.,
Pohraniční 693/31, 706 02 Ostrava - Vítkovice, Czech Republic
lucie.strilkova@mmvzyzkum.cz*

Keywords: heterogeneous weld, P23 steel, P91 steel, creep, HV10, HV0.02

1. Introduction

P23/P91 dissimilar welds are candidate joints for applications in modern boilers. Redistribution of interstitial elements (C, N), known as up-hill diffusion, represents a significant degradation mechanism of dissimilar welds during creep service. This phenomenon is controlled by activity differences of elements across the fusion boundary¹. In the vicinity of the fusion boundary the carbon/nitrogen depleted zone forms in a low alloy steel and the carbon enriched zone arises in the adjacent layer of a high alloy steel. These changes of chemical composition and microstructure occurring during the creep exposure lead to degradation of mechanical properties of dissimilar weldments.

2. Experimental material and results

Two types of dissimilar P23/P91 welds were studied. These welds were fabricated in SES Tlmače, in the Slovak Republic². For *Weld A* filler metal with chemical composition corresponding to the P91 base metal was applied. *Weld B* was made using the type P23 filler metal. Weldments were prepared by combination of the shielded metal arc welding (SMAW) and the gas tungsten arc welding (GTAW), earlier reported as TIG. The post-weld heat treatment (PWHT) of both welds was performed at 750 °C for 2 hours. Cross-weld samples for creep rupture tests involved base materials, heat affected zones and weld metal. Creep tests to rupture were carried out in air at 500, 550 and 600 °C in the stress range between 55 and 200 MPa.

Weld A (P23/WM91/P91)

The results of creep rupture tests carried out at 500 and 550 °C were close to the –20 % scatter band of standardized creep strength curve for P23 steel². The most pronounced decline of creep strength was observed during the exposure at 600 °C. The highest reduction area values were achieved in the case of specimens tested at 500 and 550 °C and the highest stresses.

Metallographical investigations revealed several localities prone to the development of creep damage. At testing temperatures of 500 and 550 °C final rupture occurred in intercritical area of the P23 heat affected zone (HAZ) or in the

fusion zone (FZ) on the side of the P23 steel – in this coarse grain area a partial decarburization took place during the both PWHT and creep exposure. After exposure at 600 °C failure locations were identified in the partly decarburized FZ on the side of the P23 steel and in some specimens in intercritical part and/or fine grain regions of the P91 HAZ. Creep damage could simultaneously develop in several parts of the weldment, often in both HAZ's of the weld. Final fracture occurred in the “weakest” locality for the given testing parameters³.

Hardness profiles were evaluated on longitudinal sections through the ruptured cross-weld specimens. Table I summarises maximum and minimum HV10 values together with their allocation for both the weldment after PWHT and for individual creep ruptured specimens. Results proved that hardness of the P91 weld metal (WM) higher than that of the P91 base metal (BM).

Table I
Maximum and minimum HV10 values and locations of their occurrence in the creep ruptured specimens, *Weld A*

Temp. [°C]	Stress [MPa]	Time to rupture, [h]	HV max.	Locality of max HV 10 measurement	HV min.	Locality of min HV 10 measurement
		after PWHT	285	CG HAZ P91	185	IC HAZ P23
500	200	18 802	339	WM	183	BM P23
550	150	9 715	287	WM	157	IC HAZ P23
550	140	8 665	281	CG HAZ P91	167	IC HAZ P23
600	110	1 384	343	WM	182	BM P23
600	100	4 056	319	WM	167	BM P23
600	90	5 171	260	WM	153	IC HAZ P23
600	75	9 852	294	WM	171	BM P23

where CG HAZ is the coarse grain part of the heat affected zone and IC HAZ is the intercritical part of the heat affected zone.

Fig. 1 shows a longitudinal section through the ruptured cross-weld specimen after creep exposure 600 °C/75 MPa/9852 h. The specimen failed in the IC part of the P91 HAZ. Microhardness profile across the WM91/ P23 interface shows hardness changes due to carbon redistribution. A big scatter in microhardness values can be attributed to the presence of creep cavities and precipitates in the metal matrix. HV0.02 values in the P91 HAZ continuously decreased from the fusion line up to the fracture line. Partial austenitization of the P91 steel in the IC HAZ was responsible for a drop and heterogeneity of hardness in this part of the HAZ. As a result, during subsequent creep exposure creep deformation was localized in this region.

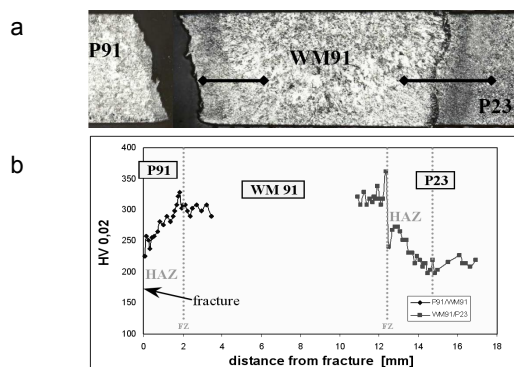


Fig. 1. Macrostructure (a) of the specimen after creep exposure 600 °C/75 MPa/9852 h and HV0.02 profiles (b) across the HAZs of the cross-weld specimen – locations are marked in (a), Weld A

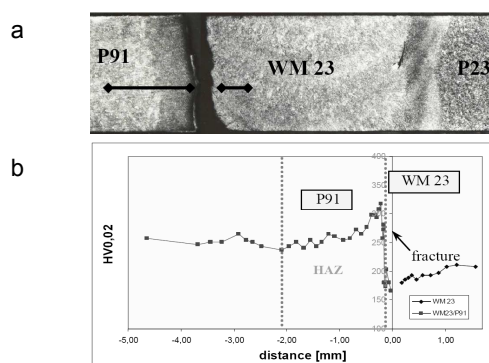


Fig. 2. Macrostructure (a) of the specimen after creep exposure 600 °C/75 MPa/6550 h and HV0.02 profiles (b) across the P91 HAZ and WM23 – locations are marked in (a), Weld B

Weld B (P23/WM23/P91)

The results of creep rupture tests performed at 500 and 550 °C were close, or slightly below the $\pm 20\%$ scatter band of standardized creep strength curve for P23 steel. The most pronounced decline of creep strength was observed, as in the case of *Weld A*, during creep exposures at 600 °C. In the course of creep at temperature of 500 °C the critical locus of the *Weld B* specimens was the IC HAZ on the side of the P23 BM. At temperatures of 550 and 600 °C the preferred failure location was the partly decarburized layer of the WM23 in the vicinity of the WM23/P91 fusion zone³. Fig. 2 shows for the specimen after creep exposure 600 °C/75 MPa/6550 h macrostructure and HV0.02 profile in the vicinity of fracture line.

Table II

Maximum and minimum HV10 values and locations of their occurrence in the ruptured creep specimens, *Weld B*

Temp. [°C]	Stress [MPa]	Time to rupture, [h]	HV max.	Locality of max HV 10 measurement	HV min.	Locality of min HV 10 measurement
		after PWHT	260	CG HAZ P91	175	IC HAZ P23
500	200	2 327	256	BM P91	183	WM, BM P23
500	170	18 679	216	CG HAZ P91	143	BM P23
550	140	6 390	236	CG HAZ P91	146	BM P23
550	125	7 778	235	BM P91	147	IC HAZ P23
600	110	1 090	238	BM P91	168	BM P23
600	100	1 538	236	BM P91	168	IC HAZ P23
600	90	2 917	216	BM P91	136	IC HAZ P23
600	75	6 550	231	BM P91	150	IC HAZ P23

Table II summarises maximum and minimum HV10 values together with their allocation for the *Weld B* after PWHT and for individual creep ruptured specimens. Hardness of the WM23 in the *Weld B* was comparable with that of the P23 BM³. The preferred failure location in *Weld B* specimens corresponded to the partly decarburized part of the WM23 adjacent to the P91 HAZ. Microhardness profile across the fusion zone in the specimen after 600 °C/75 MPa/6550 hours exposure proves hardening of the carburized P91 HAZ and at

the same time softening of the partly decarburized WM23 on the opposite side of the fusion line.

3. Conclusions

Creep rupture strength of both welds was close to the lower bound of the $\pm 20\%$ scatter band around the mean creep rupture strength curve of P23 steel. Creep damage can develop simultaneously in several parts of weldments, fracture then occurs in the “weakest” locality. Microhardness data are useful for the detection of local degradation of dissimilar welds.

The authors would like to express thanks for the financial support from the project MSM 2587080701.

REFERENCES

- Pilous V., Stránský K.: Structural Stability of Weldments for Power Plants, ČSAV Study, Academia Praha, 1989, p. 185 (in Czech).
- Vodárek V., Kuboň Z.: Proc. of 5th International Conference on Mechanics and Materials in Design, p. 267. Porto 2006.
- Vodárek V., Kuboň Z., Foret R., Hainsworth S. V.: Proc. of the IIW International Conference Safety and Reliability of Welded Components, (P. Mayr et al., ed.), pp. 233–238. Graz 2008.

L. Střílková^a, Z. Kuboň^a, and V. Vodárek^b
^a MATERIALS AND METALLURGICAL RESEARCH, Ltd.,
^b Technical University of Ostrava, Ostrava, Czech Republic):
Evaluation of Local Mechanical Properties in P23/P91 Dissimilar Welds after Creep Exposure at 500–600 °C

The experience indicates, that in majority of cases where high temperature failure of power plant components occurs, defects predominate in the vicinity of weldments. P23/P91 dissimilar welds are perspective weld joints for applications in boilers of modern power plants. This contribution deals with studies on creep behaviour and local mechanical properties of P23/P91 dissimilar welds tested at 500, 550 and 600 °C.

EFFECT OF VARIOUS GRAIN BOUNDARY PHASES AND SiC ADDITION ON THE FRACTURE CHARACTERISTICS OF Si₃N₄ BASED CERAMICS

PETER TATARKO^{a,*}, MONIKA KAŠIAROVÁ^a, JÁN DUSZA^a, and PAVOL ŠAJGALÍK^b

^a Institute of Materials Research, Slovak Academy of Sciences, Watsonova 47, 040 01 Košice, ^b Institute of Inorganic Chemistry, Slovak Academy of Sciences, Dúbravská cesta 9, Bratislava, Slovak Republic
tatarko.peter@gmail.com

Keywords: nanoindentation, silicon nitride, composite, rare-earth oxides, grain boundary phases

1. Introduction

In silicon nitride ceramics the microstructure with elongated β -Si₃N₄ grains as the reinforcing agent is a necessary but not a sufficient condition for the improvement of the fracture resistance. Silicon nitrides prepared with different densification additives and processing conditions that exhibit selfreinforced microstructures can have very different fracture resistances¹.

In silicon nitride a continuous, amorphous intergranular film is formed at the boundary between two Si₃N₄ grains and its composition varies with the oxides used as sintering additives^{2,3}. The bond strength across the interface is significantly influenced by the chemistry of the intergranular phase². This bond strength determines where the crack propagates, at the grain/intergranular phase boundary or inside the intergranular phase. Because the coefficient of thermal expansion (CTE) of the grain boundary phase varies when the sintering additives are modified, residual stresses will be a function of the chemistry at the grain boundary³. These residual stresses, together with the residual stresses introduced to the composites Si₃N₄-SiC due to the different physical properties of the silicon nitride and silicon carbide, also influence the crack propagation and the fracture toughness.

The aim of this work is to investigate the effect of various grain boundary phases and SiC addition on the local deformation and fracture characteristics of Si₃N₄ based ceramics using indentation and micro-indentation technics.

2. Experimental procedure

The starting mixtures of the set of five Si₃N₄-SiC nanocomposites consisted of the following powders: α -Si₃N₄, amorphous SiO₂, carbon black and different rare-earth oxides RE₂O₃ (RE = La, Nd, Y, Yb, or Lu). All compositions contained the same atomic amount of RE element. Amount of SiO₂ and C was calculated to achieve 5 vol.% of SiC after "in situ" carbothermal reduction process. Simultaneously, the set of five reference monolithic Si₃N₄ materials with the same composition of additives were prepared. Bulk bodies were

then hot-pressed at 1750 °C with a load of 30 MPa and 0.15 MPa pressure of nitrogen during 1 hour.

The instrumented indentation was used to yield both hardness and elastic modulus of the materials. These tests were performed using TTX-NHT nanoindentation tester (CSM Instruments, Switzerland) with a Berkovich indenter. A standard loading/unloading test mode was used with a maximum load of 100 mN and with loading/unloading rate of 200 mN min⁻¹.

The fracture toughness was measured using Vicker's indentation. The indentation fracture toughness (IF) was determined by the measurement of the crack lengths created at the load of 98 N. The fracture toughness was calculated using the equation proposed by Anstis⁴.

3. Results and discussion

All studied materials exhibited the typical bimodal microstructures composed of large elongated β -Si₃N₄ grains distributed in a fine β -Si₃N₄ matrix. Samples with a heavier (smaller) RE³⁺ cations (Y, Yb, or Lu) showed larger diameter elongated β -Si₃N₄ grains and finer β -Si₃N₄ matrix grains in comparison with the samples with a lighter (larger) RE³⁺ cations (La or Nd).

The XRD results revealed β -Si₃N₄ as a major phase and RE₂Si₂O₇ (where RE = Y, Yb or Lu) as a secondary phase in both monolithic and composite materials. This crystalline phase was not found in ceramics with La- and Nd additives. All Si₃N₄ materials also contain SiO₂ as a minor phase, whereas the Si₃N₄-SiC additionally contained SiC phase and also SiO₂, Si₂N₂O.

Fig. 1 and Fig. 2 illustrate the hardness and indentation modulus values measured at a load of 100 mN as a function of the cation size of the rare-earth elements, respectively. It is obvious that chemical composition of grain boundary phases strongly influences the values of hardness and elastic modulus of Si₃N₄ based materials. Both the hardness and the elastic modulus increased with decreasing ionic radius of RE³⁺. This is related to the fact that hardness of RE-oxynitride glasses is

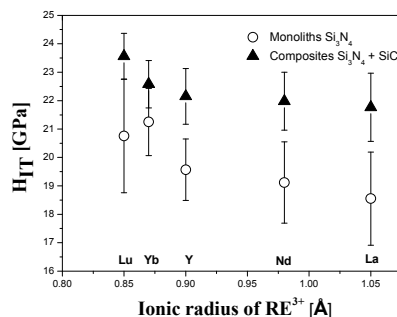


Fig. 1. Hardness values measured at a load of 100 mN

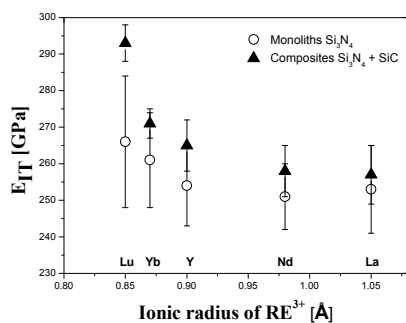


Fig. 2. Indentation modulus measured at load of 100 mN

strongly affected by nitrogen content and by the cationic field strength (CFS), which increases with decreasing ionic radius of RE³⁺. Higher hardness of composite is attributed to the finer microstructures as well as to the presence of the harder SiC particles.

It is evident that the indentation modulus values are significantly lower than the typical values of Young's modulus [317–342 GPa (ref.⁶), 280–315 GPa (ref.⁷)] for both kinds of materials given in the literature.

The values of fracture toughness also increased with decreasing ionic radius of RE³⁺ (Fig. 3). The materials doped with smaller RE exhibited higher aspect ratio of β-Si₃N₄ grains (i.e. ratio of grain length to grain width) and also higher fracture toughness in both the monoliths and the composites. This can be attributed to the fact, that toughening mechanisms were observed more frequently in the materials with higher aspect ratio.

The fracture toughness values of the composites were always lower than those of monolithic Si₃N₄ because of the finer composite microstructures. It is well known that in the case of finer microstructures there are limited possibilities for

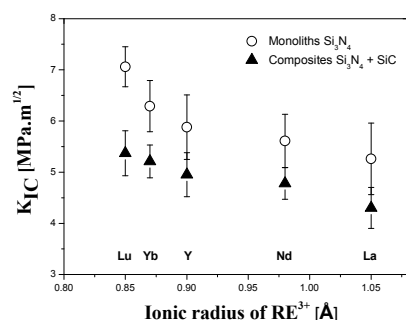


Fig. 3. Indentation fracture toughness values measured at 98 N

toughening mechanisms (crack deflection at the boundaries of elongated Si₃N₄ grains).

4. Conclusions

Influence of various grain boundary phases on the microhardness and fracture characteristics of Si₃N₄ based ceramics has been investigated. According to the results the indentation modulus as well as the indentation toughness increased with decreasing ionic radius of RE. Composites exhibited higher microhardness and indentation modulus, however lower indentation toughness in comparison with the monoliths. The indentation modulus is significantly lower than the typical values of Young's modulus for both materials.

This work was supported by VEGA 2/0156/10, by APVV 0171-06 and by LPP 0203-07.

REFERENCES

- Sun E. Y., Becher P. F., Plucknett K. P., Hsueh C.-H., Alexander K. B., Waters S. B.: *J. Am. Ceram. Soc.* **81**, 2831 (1998).
- Satet R. L., Hoffmann M. J.: *J. Am. Ceram. Soc.* **88**, 2485 (2005).
- Wang C. M., Pan X., Hoffmann M. J., Cannon R. M., Rühle M.: *J. Am. Ceram. Soc.* **79**, 788 (1996).
- Anstis G. R., Chantikul P., Lawn B. R., Marshall D. B.: *J. Am. Ceram. Soc.* **64**, 533 (1981).
- Lofaj F., Hvizdoš P., Dorčáková F., Satet R., Hoffmann M. J., de Arellano-López A. R.: *Mater. Sci. Eng. A357*, 181 (2003).
- Guo S., Hirotsaki N., Yamamoto Y., Nishimura T., Mitomo M.: *J. Eur. Ceram. Soc.* **23**, 537 (2003).
- Miyazaki H., Hyuga H., Yoshizawa Y., Hirao K., Ohji T.: *J. Eur. Ceram. Soc.* **29**, 1535 (2009).

P. Tatarko^a, M. Kašiarová^a, J. Dusza^a, and P. Šajgalík^b (^a*Institute of Materials Research, SAS, Košice;* ^b*Institute of Inorganic Chemistry, SAS, Bratislava, Slovakia*): **Effect of Various Grain Boundary Phases and SiC Addition on The Fracture Characteristics of Si₃N₄ Based Ceramics**

Effect of various grain boundary phases and SiC addition on fracture characteristics of the Si₃N₄ based ceramics has been investigated by indentation technics. Strong influence of different rare-earth oxide additives on the hardness, indentation modulus and indentation toughness was found in both the Si₃N₄-SiC composites and Si₃N₄ monoliths. These values increased with decreasing ionic radius of rare-earth elements. Composites exhibited the higher hardness and elastic modulus values compared to monoliths, while monoliths exhibited higher values of fracture toughness.

MICROSTRUCTURAL AND MICROMECHANICAL STUDY OF GYPSUM

PAVEL TESÁREK*, and **JIŘÍ NĚMEČEK**

*Czech Technical University in Prague, Thákurova 7, 166 29
Prague, Czech Republic
pavel.tesarek@fsv.cvut.cz*

Keywords: nanoindentation, gypsum, micromechanical properties, deconvolution

1. Introduction

Gypsum is a structural material known for several thousands years which is commonly used for building purposes. Hardened material consists of two components – gypsum and water. In general, it is assumed that properties of gypsum, its hydration and hardening is well-known due to its relatively simple chemistry compared to more complicated systems like in case of e.g. cement. However, similar chemical composition of two gypsum mixtures can result in very different behavior and properties¹. Many authors take gypsum as simple two-component system for modeling of hardening processes and other effects like water to gypsum ratio, porosity on macroscopic properties of gypsum².

From the chemistry point of view, every gypsum binder is composed of three main components – calcium sulphate anhydrite (CaSO_4) in different modifications, calcium sulphate hemihydrate ($\text{CaSO}_4 \cdot \frac{1}{2}\text{H}_2\text{O}$) – α - or β -gypsum, and calcium sulphate dihydrate ($\text{CaSO}_4 \cdot 2\text{H}_2\text{O}$)¹. The gypsum binder consists also some impurities and additives in case of natural sources.

As mentioned above, other effects than chemical composition can affect on the resulting behavior of the hardened gypsum. Therefore, it is necessary to take into account macrostructural properties³ as well as microstructural effects⁴ (amount of bound water, crystal orientation, porosity, etc.) for predicting and modeling of macroscopic properties. Our aim was to describe micromechanical behavior of hardened gypsum on a simplified model system consisting of a low-porosity α -gypsum which is used for dental purposes⁵. Although, the dental gypsum will probably never be used in building industry, it is assumed that its microstructure (e.g. crystallography) and mechanical properties are analogous to the real structural gypsums (that are mainly composed of β -gypsums).

2. Materials and tested samples

Commercially available dental gypsum Interdent[®] (with compressive strength 250 MPa after 24 hours) was used in our study. It was assumed that water to gypsum (w/g) ratio will have influence on its micromechanical properties. Therefore, five different types of samples with w/g=0.18, 0.19, 0.20, 0.21 and 0.22, further denoted as G0, G1, G2, G3 and G4, were prepared. Fig. 1 shows typical sample surface after polishing

with easily visible large capillary pores (in black). Lighter parts in Fig. 1 and Fig. 2 are composed of non-hydrated gypsum grains.

3. Nanoindentation

Micromechanical properties of samples were measured using CSM Nanohardness tester. Each sample was tested on arbitrary position by a rectangular grid of $\sim 12 \times 15 = 180$ indents. Quasi-static loading consisted of 10 s of linear loading (rate 30 mN min^{-1}), 10 s of holding period at constant peak force 5 mN and 10 s of unloading (rate 30 mN min^{-1}). The distance between individual indents was set $15 \mu\text{m}$ to avoid mutual influences. The size of the tested area $165 \times 210 \mu\text{m}$ was considered to be representative enough and to contain all solid material phases for this particular case.

Elastic constants (Young's modulus) were evaluated for individual indents by standard Oliver and Pharr methodology³. Poisson's ratio was estimated to be 0.2 (Ref.³⁻⁶) for all cases.

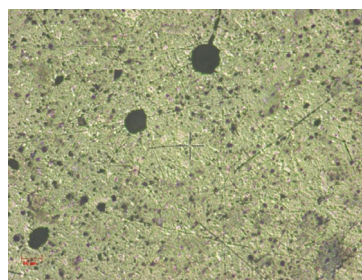


Fig. 1. Optical image of a gypsum sample G2 with w/g = 0.2 (capillary porosity appears as black circles, non-hydrated gypsum particles are light colored)



Fig. 2. High magnification optical image of a gypsum sample G2 with w/g = 0.2 (indentation imprints are in circles)

4. Evaluation of experimental results

Evaluated Youngs' moduli E were merged for each sample and analyzed statistically. Results in the form of probability density function are depicted in Fig. 3. Significant peak of

E appears around ~40 GPa which is considered to be characteristic value for a dominant part of the system. Minor peaks can be found around ~20 GPa (lower stiffness phases) and ~60 GPa (higher stiffness phases, probably non-hydrated grains). As the w/g ratio increases slight shift towards lower E can be found in Fig. 3, especially for G4 sample. This could show on the effect of increased porosity caused by higher water amount.

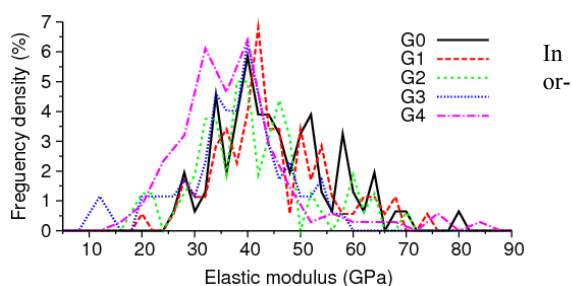


Fig. 3. Experimental probability density function of Young's modulus for all tested gypsum samples

der to better characterize the differences in E between the samples, deconvolution procedure^{6,7} was employed. The ill-posed problem of deconvolution was determined by a fixed number of phases. The number was set to three which corresponds to one lower stiffness, one dominant and one higher stiffness phase, respectively. In case of G0 and G4 the lower stiffness phase is almost lacking, so the deconvolution was

Table I
Elastic moduli and volume fractions from deconvolution

Materials	Phase	Mean [GPa]	St. Dev. [GPa]	Vol. frac.
G0 w/g=0.18	1	-	-	0
	2	38.283	5.109	0.656
	3	58.360	9.656	0.344
G1 w/g=0.19	1	20.209	1.837	0.023
	2	40.892	6.689	0.801
	3	60.674	6.939	0.176
G2 w/g=0.20	1	19.357	3.539	0.044
	2	37.234	5.189	0.713
	3	56.278	11.803	0.244
G3 w/g=0.21	1	19.788	4.740	0.103
	2	39.910	6.283	0.845
	3	58.805	6.035	0.052
G4 w/g=0.22	1	-	-	0
	2	35.871	7.295	0.884
	3	62.905	10.516	0.116

Note: 1 ≈ lower stiffness phase; 2 ≈ dominant phase; 3 ≈ higher stiffness phase.

performed just for two phases (dominant and higher stiffness). Results from deconvolution in the form of mean phase values and volume fractions are given in Tab. I.

It can be seen in Tab. I that the E-value of the dominant phase lies between ~36 to 41 GPa. Also, the volume fractions of the dominant phase are similar for all samples (65–88 %). From the micromechanical point of view it seems that the samples are very similar, too. There was no substantial difference found in the elasticity of all tested samples.

It can be assumed from the above results that macromechanical differences in elasticity of the samples with different water to gypsum ratios are caused by effects which take place on a higher level, e.g. large capillary porosity (Fig. 1).

5. Conclusions

Based on statistical evaluation of nanoindentation experiments and subsequent deconvolution it was found that gypsum samples exhibit similar micromechanical behavior in terms of elasticity of their dominant phases.

Support of the Ministry of Education of the Czech Republic (project MSM 6840770003) and the Czech Science Foundation (GAČR 103/09/1748) is gratefully acknowledged.

REFERENCES

- Garg M., Jain N., Singh M.: *Constr. Build. Mater.* 23 (2009).
- Šatava V.: *Ceramics – Silikáty*, 40, 2 (1996).
- Oliver W., Pharr G.: *J. Mater. Res.* 7 (1992).
- Arslan A. T., Koca M., Aydogmus Y. T., Klapperich H., Yılmaz H. R.: *Rock Mech. Rock Engng.* 41 (2008).
- Singh M.: *Constr. Build. Mater.* 19 (2005).
- Němeček J., Lukeš J.: *Chem. Listy* 104, (2010).
- Němeček J., Šmilauer V., Kopecký L., accepted for publication in *Cem. & Concr. Comp.*, ISSN: 0958-9465.

P. Tesárek, and J. Němeček (*Czech Technical University in Prague, Faculty of Civil Engineering, Czech Republic*): **Microstructural and Micromechanical Properties of Gypsum**

Gypsum samples (dental gypsum Interdent[®]) with different water to gypsum ratios have been investigated with nanoindentation. Statistical evaluation and deconvolution into several phases showed on similar micromechanical behavior of all samples. Elastic modulus of the dominant phase which occupies 65–88 % of the sample volume reaches average values ~36–41 GPa.